Communication

Spectral MoM NUFFT-Based Formulation for the Efficient Analysis of High-Order Bandpass FSSs With Tightly Packed Nonresonant Elements in Skewed Grid

Juan Córcoles and Rafael R. Boix

***Abstract*— This communication presents a formulation of the spectral-domain Method of Moments (spectral MoM) for the analysis of periodic multilayered structures with a number of metallized interfaces alternating patches and apertures. Edge singularity entire-domain basis functions are used to model the electric currents on the patches and the tangential electric fields in the apertures. The formulation is especially suitable to characterize high-order bandpass frequency selective surfaces (FSSs) made up of nonresonant elements. Also in this communication, the nonuniform fast Fourier transform (NUFFT) is used in the spectral MoM to cover the case of unit cells in skewed grids, which enables the analysis of nonrectangular periodic lattices with tightly packed elements. Numerical examples of the design of third-order and fifth-order bandpass FSSs are presented. The FSSs are made up of hexagonal patches and apertures arranged in an equilateral triangular lattice. Results are cross-checked against commercial software CST Microwave Studio (CST MWS), and excellent agreement is found, our in-house software being more than one order of magnitude faster than CST MWS. This CPU time saving makes the proposed formulation very convenient for full-wave optimization and design.**

***Index Terms*— Fourier transforms, frequency selective surfaces (FSSs), moment methods, multilayered media, periodic structures.**

I. Introduction

The spectral-domain Method of Moments (spectral MoM) is a long-known, widely used technique to analyze planar frequency selective surfaces (FSSs) [1]–[3]. In this method, with the objective of alleviating the computational burden, entire-domain basis functions [2] with edge singularities [1], [4] are employed in the spatial domain to approximate electric/magnetic currents inside conducting/aperture elements with canonical shape. This ensures a fast convergence of the spectral MoM with respect to the number of basis functions [4]. One successful strategy for the extension of edge-singularity basis functions to more complex shapes is presented in [5]. However, closed forms for the Fourier transforms of these basis functions are not available, in general, and numerical procedures are required to compute their spectral counterpart. Recently, the nonuniform fast Fourier transform (NUFFT) has been introduced as a numerical tool for the determination of these Fourier transforms in periodic structures with rectangular unit cells [6]. The NUFFT allows an adaptive sampling within the conducting/aperture geometry, which is more accurate than the standard rectangular sampling provided by the regular FFT.

Solid-interior type conducting/aperture FSS elements usually exhibit a nonresonant behavior (as opposed to loop type elements, which are resonant) [3]. Therefore, they are usually referred to as capacitive patches and inductive apertures because of their analogous circuital response. Although solid-interior type elements have not traditionally been among the top choices to implement bandpass FSSs, a few years ago Al-Joumayly and Behdad reported the design of high-order bandpass FSSs made up of a multilayered structure where capacitive patches alternate with inductive apertures [7]. These FSSs have the advantage that they are electrically thin and their periodicities are a small fraction of the free-space wavelength, which makes the FSSs quite insensitive to changes in the polarization and angle of the incident electromagnetic (EM) waves. Although the application of the spectral MoM to analyze arrays of stacked patches [8] or coupled apertures [5] embedded in a multilayered structure is of common practice, works where apertures mix with patches are usually limited to one or two layers, mostly based on the pioneer formulation found in [9].

This communication first proposes a specific formulation for the spectral MoM analysis of a periodic multilayered structure with an arbitrary number of alternating patches and apertures. The formulation is based on the transverse propagation matrix relating electric currents and electric fields at the interfaces [10], and it can be considered to be a generalization of [9]. Because of the alternating nature of patches and apertures, the formulation is especially indicated for the analysis of multilayered bandpass FSSs made up of nonresonant elements [7]. Also in the communication, the NUFFT for the spectral MoM [6] is extended to analyze the case of skewed grids. This follows the recommendations of Munk, who suggests that a way to relieve the impact of solid-interior type elements on FSS design is their arrangement in nonrectangular lattices to tightly pack them [3]. Finally, as a practical application of the proposed formulation, we present numerical examples of design of third-order and fifth-order bandpass FSSs made up of hexagonal patches and apertures, which are arranged in an equilateral triangular lattice. These particular examples show that the formulation proposed in the communication has potential use in full-wave optimization and design of FSSs owing to its computational efficiency.

II. Proposed Formulation

In the following, $\{\cdot\}$ and $[\cdot]$ will denote, respectively, column vectors and matrices. As particular cases, $\tilde{\cdot}$ will denote a 2-D column vector whose entries account for the x and y component of a transverse (to z) geometrical vector, while $\bar{\bar{\cdot}}$ will denote a 2×2 dyadic tensor which relates two 2-D vectors. Straight bold fonts will denote quantities in the discrete 2-D Fourier transform domain,

Manuscript received October 19, 2020; revised December 28, 2020; accepted January 31, 2021. Date of publication March 1, 2021; date of current version September 3, 2021. This work was funded by Fondo Europeo de Desarrollo Regional (FEDER)/Ministerio de Ciencia e Innovación–Agencia Estatal de Investigación/TEC2017-84724-P and TEC2016-76070-C3-1-R. *(Corresponding author: Juan Córcoles.)*

Juan Córcoles is with the Department of Electronic and Communications Technology, School of Engineering (Escuela Politécnica Superior), Universidad Autónoma de Madrid, 28049 Madrid, Spain (e-mail: juan.corcoles@uam.es).

Rafael R. Boix is with the Microwaves Group, Department of Electronics and Electromagnetism, College of Physics, University of Seville, 41012 Seville, Spain (e-mail: boix@us.es).

Color versions of one or more figures in this communication are available at https://doi.org/10.1109/TAP.2021.3061138.

Digital Object Identifier 10.1109/TAP.2021.3061138

0018-926X © 2021 IEEE. Personal use is permitted, but republication/redistribution requires IEEE permission.
See https://www.ieee.org/publications/rights/index.html for more information.

Authorized licensed use limited to: Universidad de Sevilla. Downloaded on July 23,2024 at 15:02:16 UTC from IEEE Xplore. Restrictions apply.

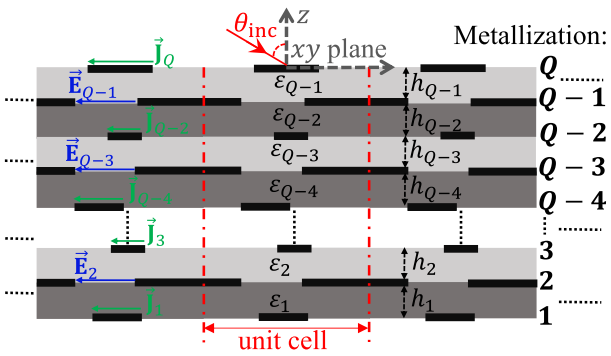

Fig. 1. Side view of the multilayered structure to be analyzed.

which depend on the two discrete Fourier variables (k_x^{mn}, k_y^{mn}). This spectral domain dependence will be usually dropped and implicitly assumed. Italic bold fonts will denote quantities in the spatial domain, which depend on the two variables (x, y). Again, this spatial domain dependence will be usually dropped and implicitly assumed. A time dependence of the type $e^{j\omega t}$ will be assumed and suppressed throughout.

A. Spectral MoM for Arbitrary Number of Alternating Patches and Apertures Embedded in Multilayered Dielectric Media

A side view of the periodic structure to be analyzed is shown in Fig. 1. It consists of Q metallizations levels placed at the interfaces of a multilayered dielectric medium perpendicular to the z-axis, which is assumed to be infinite in the x- and y-directions. The metallizations are assumed to be perfect electric conductors (PECs) of negligible thickness. Each dielectric layer has a complex permittivity $\varepsilon_q = \varepsilon_0\varepsilon_{rq}(1 - j\tan\delta_q)$ and a thickness h_q (the magnetic permeability is considered to be μ_0 in all space). Within the unit cell, along the z-axis, each patch is followed by an aperture and each aperture is followed by a patch. Without loss of generality, the structure in Fig. 1 considers that both the first and the last (Qth) metallization levels are made of patches, thus resulting in Q being an odd number. This way, the qth metallization level is a patch if $q \in \mathbb{O}$ or an aperture if $q \in \mathbb{E}$, where $\mathbb{O}$ and $\mathbb{E}$ stand for the set of, respectively, the odd and even natural numbers. Please note that the following analysis is valid for other different cases of first and last metallization levels, as long as patches alternate with apertures along the z-axis.

Let us assume an EM plane wave with propagation direction $(\theta_{\text{inc}}, \phi_{\text{inc}})$ impinges on the multilayered structure from the $z > 0$ half-space. Assuming an operation frequency that ensures the absence of grating lobes, the periodic structure of Fig. 1 will generate an EM reflected plane wave propagating toward the $z > 0$ half-space in the specular reflection direction, and an EM transmitted plane wave propagating toward the $z < -\sum_{q=1}^{Q-1} h_q$ half-space in the direction of the incident wave. The objective of the application of the spectral MoM is the computation of the reflection power coefficient, R_{00}, as the ratio between the power carried by the reflected wave and that carried by the incident wave, and also the computation of the transmission power coefficient, T_{00}, as the ratio between the power carried by the transmitted wave and that carried by the incident wave [11].

In the spectral domain, the structure of Fig. 1 can be characterized in matrix form through (1), as shown at the bottom of the page, (see [10, eq. 5]), where every 2×2 matrix $\tilde{\mathbf{L}}_{q,p}$ relates the electric current $\vec{\mathbf{J}}_q$ and the tangential electric field $\vec{\mathbf{E}}_p$ at, respectively, the qth and pth metallized interfaces by assuming the rest of metallized interfaces are substituted by PEC planes. This transverse propagation matrix can be computed by means of the recurrent algorithm described in [10]. For the sake of clarity, Fig. 1 only shows one dielectric medium between metallizations, though the inclusion of an arbitrary number of dielectric layers between two consecutive metallization levels can be easily accomplished within this algorithm.

The approximation of $\vec{\mathbf{E}}_q$ in (1) with basis functions, followed by Galerkin's method, would lead to the application of the spectral MoM for multilayered arrays of coupled apertures [5]. In a similar manner, by taking the inverse of the matrix system in (1), the so-called spectral dyadic Green's function can be readily computed [10], and in this case the approximation of $\vec{\mathbf{J}}_q$ with basis functions will eventually lead to the spectral MoM for multilayered arrays of stacked patches [8]. However, for the application of the spectral MoM to the structure shown in Fig. 1, it is convenient to approximate $\vec{\mathbf{J}}_q$ for $q \in \mathbb{O}$ (patches) and $\vec{\mathbf{E}}_q$ for $q \in \mathbb{E}$ (apertures), thus requiring a matrix relation in the form

$$\begin{Bmatrix} \vec{\mathbf{E}}_Q \\ \vec{\mathbf{J}}_{Q-1} \\ \vdots \\ \vec{\mathbf{J}}_{q+1} \\ \vec{\mathbf{E}}_q \\ \vec{\mathbf{J}}_{q-1} \\ \vdots \\ \vec{\mathbf{J}}_2 \\ \vec{\mathbf{E}}_1 \end{Bmatrix} = \begin{bmatrix} \tilde{\boldsymbol{\Xi}}_{Q,Q} & \cdots & \tilde{\boldsymbol{\Xi}}_{Q,1} \\ \vdots & \ddots & \vdots \\ \vdots & \ddots & \vdots \\ \vdots & \tilde{\boldsymbol{\Xi}}_{q,q} & \vdots \\ \vdots & \ddots & \vdots \\ \vdots & \ddots & \vdots \\ \tilde{\boldsymbol{\Xi}}_{2,Q} & \cdots & \tilde{\boldsymbol{\Xi}}_{2,1} \\ \tilde{\boldsymbol{\Xi}}_{1,Q} & \cdots & \tilde{\boldsymbol{\Xi}}_{1,1} \end{bmatrix} \begin{Bmatrix} \vec{\mathbf{J}}_Q \\ \vec{\mathbf{E}}_{Q-1} \\ \vdots \\ \vec{\mathbf{E}}_{q+1} \\ \vec{\mathbf{J}}_q \\ \vec{\mathbf{E}}_{q-1} \\ \vdots \\ \vec{\mathbf{E}}_2 \\ \vec{\mathbf{J}}_1 \end{Bmatrix}. \tag{2}$$

To compute the matrix entries in (2), we solve from (1) for the required relations between all $\vec{\mathbf{E}}_q$ and $\vec{\mathbf{J}}_q$ in (2). After some simple but careful algebraic operations, we can arrive at

$$\vec{\mathbf{E}}_q = -\tilde{\mathbf{L}}_{q,q}^{-1}\tilde{\mathbf{L}}_{q,q-1}\vec{\mathbf{E}}_{q-1} + \tilde{\mathbf{L}}_{q,q}^{-1}\vec{\mathbf{J}}_q - \tilde{\mathbf{L}}_{q,q}^{-1}\tilde{\mathbf{L}}_{q,q+1}\vec{\mathbf{E}}_{q+1},\ q \in \mathbb{O} \tag{3}$$

$$\begin{aligned} \vec{\mathbf{J}}_q = {} & -\tilde{\mathbf{L}}_{q,q-1}\tilde{\mathbf{L}}_{q-1,q-1}^{-1}\tilde{\mathbf{L}}_{q-1,q-2}\vec{\mathbf{E}}_{q-2} + \tilde{\mathbf{L}}_{q,q-1}\tilde{\mathbf{L}}_{q-1,q-1}^{-1}\vec{\mathbf{J}}_{q-1} \\ & + \big(\tilde{\mathbf{L}}_{q,q} - \tilde{\mathbf{L}}_{q,q-1}\tilde{\mathbf{L}}_{q-1,q-1}^{-1}\tilde{\mathbf{L}}_{q-1,q} \\ & \quad - \tilde{\mathbf{L}}_{q,q+1}\tilde{\mathbf{L}}_{q+1,q+1}^{-1}\tilde{\mathbf{L}}_{q+1,q}\big)\vec{\mathbf{E}}_q \\ & + \tilde{\mathbf{L}}_{q,q+1}\tilde{\mathbf{L}}_{q+1,q+1}^{-1}\vec{\mathbf{J}}_{q+1} \\ & - \tilde{\mathbf{L}}_{q,q+1}\tilde{\mathbf{L}}_{q+1,q+1}^{-1}\tilde{\mathbf{L}}_{q+1,q+2}\vec{\mathbf{E}}_{q+2},\ q \in \mathbb{E} \end{aligned} \tag{4}$$

$$\begin{Bmatrix} \vec{\mathbf{J}}_Q \\ \vdots \\ \vec{\mathbf{J}}_q \\ \vdots \\ \vec{\mathbf{J}}_2 \\ \vec{\mathbf{J}}_1 \end{Bmatrix} = \begin{bmatrix} \tilde{\mathbf{L}}_{Q,Q} & \tilde{\mathbf{L}}_{Q,Q-1} & \tilde{\mathbf{0}} & \cdots & \tilde{\mathbf{0}} & \tilde{\mathbf{0}} & \tilde{\mathbf{0}} & \tilde{\mathbf{0}} & \tilde{\mathbf{0}} & \cdots & \tilde{\mathbf{0}} & \tilde{\mathbf{0}} & \tilde{\mathbf{0}} \\ \vdots & \vdots & \vdots & \ddots & \vdots & \vdots & \vdots & \vdots & \vdots & \ddots & \vdots & \vdots & \vdots \\ \tilde{\mathbf{0}} & \tilde{\mathbf{0}} & \tilde{\mathbf{0}} & \cdots & \tilde{\mathbf{0}} & \tilde{\mathbf{L}}_{q,q+1} & \tilde{\mathbf{L}}_{q,q} & \tilde{\mathbf{L}}_{q,q-1} & \tilde{\mathbf{0}} & \cdots & \tilde{\mathbf{0}} & \tilde{\mathbf{0}} & \tilde{\mathbf{0}} \\ \vdots & \vdots & \vdots & \ddots & \vdots & \vdots & \vdots & \vdots & \vdots & \ddots & \vdots & \vdots & \vdots \\ \tilde{\mathbf{0}} & \tilde{\mathbf{0}} & \tilde{\mathbf{0}} & \cdots & \tilde{\mathbf{0}} & \tilde{\mathbf{0}} & \tilde{\mathbf{0}} & \tilde{\mathbf{0}} & \tilde{\mathbf{0}} & \cdots & \tilde{\mathbf{L}}_{2,3} & \tilde{\mathbf{L}}_{2,2} & \tilde{\mathbf{L}}_{2,1} \\ \tilde{\mathbf{0}} & \tilde{\mathbf{0}} & \tilde{\mathbf{0}} & \cdots & \tilde{\mathbf{0}} & \tilde{\mathbf{0}} & \tilde{\mathbf{0}} & \tilde{\mathbf{0}} & \tilde{\mathbf{0}} & \cdots & \tilde{\mathbf{0}} & \tilde{\mathbf{L}}_{1,2} & \tilde{\mathbf{L}}_{1,1} \end{bmatrix} \begin{Bmatrix} \vec{\mathbf{E}}_Q \\ \vdots \\ \vec{\mathbf{E}}_q \\ \vdots \\ \vec{\mathbf{E}}_2 \\ \vec{\mathbf{E}}_1 \end{Bmatrix} \tag{1}$$

Authorized licensed use limited to: Universidad de Sevilla. Downloaded on July 23,2024 at 15:02:16 UTC from IEEE Xplore. Restrictions apply.

where the terms with $q \pm 1$ and $q \pm 2$ are not actually present when their values are lower than 1 or higher than Q (i.e., the cases $q = 1, 2, Q-1, Q$). Direct inspection of (2)–(4) provide the values $\tilde{\boldsymbol{\Xi}}_{p,q}$ in (2), where, as expected from the structure in Fig. 1, it should be remarked that $\tilde{\boldsymbol{\Xi}}_{p,q} = \tilde{\mathbf{0}}$ for $p < q-1$ and $p > q+1$ if $q \in \mathbb{O}$, while $\tilde{\boldsymbol{\Xi}}_{p,q} = \tilde{\mathbf{0}}$ for $p < q-2$ and $p > q+2$ if $q \in \mathbb{E}$.

In order to determine the reflection and transmission power coefficients, R_{00} and T_{00}, for the structure of Fig. 1, the quantities $\vec{\mathbf{J}}_q$ ($q \in \mathbb{O}$) and $\vec{\mathbf{E}}_q$ ($q \in \mathbb{E}$) have to be approximated in terms of known basis functions $\vec{\mathbf{f}}_{q,n_q}$ and corresponding degrees of freedom (d.o.f.) d_{q,n_q} as

$$\vec{\mathbf{J}}_q = \sum_{n_q=1}^{N_q} d_{q,n_q} \vec{\mathbf{f}}_{q,n_q}, q \in \mathbb{O}, \quad \vec{\mathbf{E}}_q = \sum_{n_q=1}^{N_q} d_{q,n_q} \vec{\mathbf{f}}_{q,n_q}, q \in \mathbb{E} \quad (5)$$

where N_q stands for the total number of basis functions used at the qth metallization level.

Then, the final spectral MoM system of linear equations $[\boldsymbol{\Gamma}]\{\mathbf{d}\} = \{\mathbf{e}\}$ is built, $\{\mathbf{d}\}$ being a vector containing all d.o.f. in the problem. For that purpose, we introduce (5) into (2) and apply Galerkin's method in the spectral domain [1] to arrive at (the dependence of (k_x^{mn}, k_y^{mn}) is now explicitly stated)

$$\Gamma_{q,n_q}^{p,n_p} = \sum_{m=-\infty}^{+\infty} \sum_{n=-\infty}^{+\infty} \vec{\mathbf{f}}_{p,n_p}(k_x^{mn}, k_y^{mn}) \cdot \tilde{\boldsymbol{\Xi}}_{p,q}(k_x^{mn}, k_y^{mn}) \vec{\mathbf{f}}_{q,n_q}(k_x^{mn}, k_y^{mn}) \quad (6)$$

$$e^{p,n_p} = -\vec{\mathbf{f}}_{p,n_p}(k_x^{00}, k_y^{00}) \cdot \begin{cases} \vec{\boldsymbol{E}}_p^{0,\mathrm{ab}}, & p \in \mathbb{O} \\ \vec{\boldsymbol{J}}_p^{0,\mathrm{ab}}, & p \in \mathbb{E}. \end{cases} \quad (7)$$

In (6) and (7), the superscript p, n_p of Γ_{q,n_q}^{p,n_p} corresponds to row index $n_p + \sum_{p'=1}^{p-1} N_{p'}$ in $[\boldsymbol{\Gamma}]$ and $\{\mathbf{e}\}$, respectively, while a similar rationale applies to the subscript q, n_q of Γ_{q,n_q}^{p,n_p} for the column index in $[\boldsymbol{\Gamma}]$. In (6) and (7), $\cdot$ stands for the scalar product between two $\mathbb{C}^2$ vectors (i.e., including the complex conjugate for the first one). Finally, in (7), $\vec{\boldsymbol{E}}_p^{0,\mathrm{ab}}$ and $\vec{\boldsymbol{J}}_p^{0,\mathrm{ab}}$ stand for the complex amplitude of, respectively, the electric field and the electric current, in the situation where patches and apertures are absent (i.e., no metal for $p \in \mathbb{O}$ and all metal for $p \in \mathbb{E}$).

Once the MoM system of equations is solved for a given incident EM plane wave, electric fields of the reflected and transmitted plane waves in the absence of grating lobes can be straightforwardly computed, respectively, in terms of the first and the last row in (2) by using (5). Then, R_{00} and T_{00} can be readily obtained in terms of these reflected and transmitted electric fields (see [11, Sec. II-B] for details).

B. NUFFT of Basis Functions in Skewed Grids

Let us assume the unit cell of the periodic structure of Fig. 1 is an arbitrary parallelogram belonging to a generic skewed grid, as shown in red in Fig. 2(a). The lower-left corner of the parallelogram is placed at $(x, y) = (0, 0)$, with sides a and b forming an angle of, respectively, α_1 and α_2 upward with the x-axis. For this type of lattice, the spectral variables (k_x^{mn}, k_y^{mn}) introduced in (6) and (7) take the form [2]

$$k_x^{mn} = k_{x0} + m\frac{2\pi b}{A}\sin\alpha_2 - n\frac{2\pi a}{A}\sin\alpha_1 \quad (8)$$

$$k_y^{mn} = k_{y0} - m\frac{2\pi b}{A}\cos\alpha_2 + n\frac{2\pi a}{A}\cos\alpha_1 \quad (9)$$

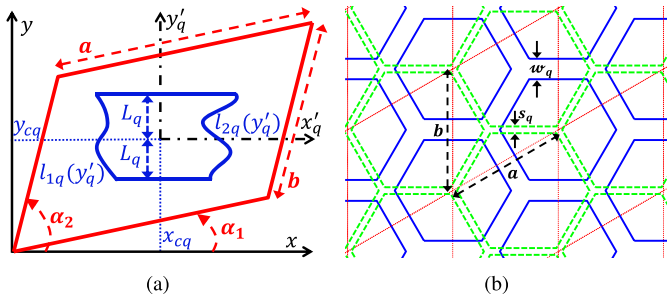

Fig. 2. (a) Nonrectangular unit cell for a generic skewed grid (red) and contour (blue) of the element (patch or aperture) inside the unit cell at the qth metallization level. (b) Arrangement of alternating hexagonal patches (dashed green) and apertures (solid blue) and corresponding unit cells (dotted red) for a lattice made of equilateral triangles.

where $k_{x0} = k_0 \sin\theta_{\mathrm{inc}} \cos\phi_{\mathrm{inc}}$, $k_{y0} = k_0 \sin\theta_{\mathrm{inc}} \cos\phi_{\mathrm{inc}}$, k_0 is the free-space wavenumber and A is the unit cell area, given by

$$A = ab\sin(\alpha_2 - \alpha_1). \quad (10)$$

The contour of a patch for $q \in \mathbb{O}$ or an aperture for $q \in \mathbb{E}$ is shown in blue in Fig. 2(a). This contour is bounded at $y'_q = \pm L_q$ for the local coordinate system (x'_q, y'_q) whose origin is set to $(x, y) = (x_{cq}, y_{cq})$. The leftmost and rightmost boundaries are defined, respectively, by parametrization functions $x'_q = l_{1q}(y'_q)$ and $x'_q = l_{2q}(y'_q)$. Without loss of generality, there can be more than one patch/aperture in the unit cell [6], though we will restrain our exposition to the case where only one patch/aperture is present.

To approximate $\vec{\boldsymbol{J}}_q(x, y)$ inside patches for $q \in \mathbb{O}$ and $\vec{\boldsymbol{E}}_q(x, y)$ inside apertures for $q \in \mathbb{E}$ within the region bounded by this contour, we make use of the auxiliary functions $\vec{\boldsymbol{\zeta}}_{q,n_q}(x'_q, y'_q)$ ($n_q = 1, \ldots, N_q$) defined below

$$\vec{\boldsymbol{\zeta}}_{q,i}(x'_q, y'_q) = \frac{1}{l_q^-(y'_q)} \frac{T_{r_1-1}(\chi_q)}{\sqrt{1-\chi_q^2}} U_{s_1-1}(\varphi_q)\sqrt{1-\varphi_q^2} \times \left(\hat{\boldsymbol{x}}\left(\chi_q \frac{\mathrm{d}l_q^-(y'_q)}{\mathrm{d}y'_q} + \frac{\mathrm{d}l_q^+(y'_q)}{\mathrm{d}y'_q}\right) + \hat{\boldsymbol{y}}\right) \quad (11)$$

$$\vec{\boldsymbol{\zeta}}_{q,j+N_q^{1r}N_q^{1s}}(x'_q, y'_q) = \frac{1}{L_q} U_{r_2-1}(\chi_q)\sqrt{1-\chi_q^2} \frac{T_{s_2-1}(\varphi_q)}{\sqrt{1-\varphi_q^2}} \hat{\boldsymbol{x}} \quad (12)$$

$$\chi_q = \frac{x'_q - l_q^+(y'_q)}{l_q^-(y'_q)}, \quad \varphi_q = \frac{y'_q}{L_q}, \quad l_q^{\pm}(y'_q) = \frac{l_{1q}(y'_q) \pm l_{2q}(y'_q)}{2} \quad -L_q \le y'_q \le L_q, \quad l_{1q}(y'_q) \le x'_q \le l_{2q}(y'_q) \quad (13)$$

where T_n and U_n stand for nth order Chebychev polynomials of first and second kind, respectively, and where $r_1 = 1, \ldots, N_q^{1r}$, $s_1 = 1, \ldots, N_q^{1s}$, $r_2 = 1, \ldots, N_q^{2r}$, $s_2 = 1, \ldots, N_q^{2s}$, $i = 1, \ldots, N_q^{1r}N_q^{1s}$, $j = 1, \ldots, N_q^{2r}N_q^{2s}$ and $N_q = N_q^{1r}N_q^{1s} + N_q^{2r}N_q^{2s}$. The basis functions of (11) and (12) were introduced in [5] to model magnetic currents on apertures because they account for the singularities of the magnetic currents at the edges of the apertures. Bearing in mind that the edge singularities of the electric currents on the patches are the same as those of the magnetic currents on the apertures, and taking the definition of magnetic currents on apertures into account, the basis functions for $\vec{\boldsymbol{J}}_q$ and $\vec{\boldsymbol{E}}_q$ (see the spectral counterpart in (5)) are chosen as

$$\vec{\boldsymbol{f}}_{q,n_q} = \vec{\boldsymbol{\zeta}}_{q,n_q}, q \in \mathbb{O}, \quad \vec{\boldsymbol{f}}_{q,n_q} = \hat{\boldsymbol{z}} \times \vec{\boldsymbol{\zeta}}_{q,n_q}, q \in \mathbb{E}. \quad (14)$$

Authorized licensed use limited to: Universidad de Sevilla. Downloaded on July 23,2024 at 15:02:16 UTC from IEEE Xplore. Restrictions apply.

The functions $\vec{f}_{q,n_q}(x, y)$ are defined as $\vec{f}_{q,n_q}(x'_q, y'_q)$ if $-L_q \leq y'_q \leq L_q$ and $l_{1q}(y'_q) < x'_q < l_{2q}(y'_q)$, and $\vec{\mathbf{0}}$ elsewhere. The Fourier transforms take the form

$$\vec{\mathbf{f}}_{q,n_q}\left(k_x^{mn}, k_y^{mn}\right) = \frac{1}{A}\iint_A \vec{f}_{q,n_q}(x, y)\mathrm{e}^{-j\left(k_x^{mn}x + k_y^{mn}y\right)}\mathrm{d}x\mathrm{d}y. \quad (15)$$

By carrying out a change of variable $(x'_q, y'_q) = (x, y) - (x_{cq}, y_{cq})$ and using (8) and (9), we can arrive after some operations at the following expression for (15):

$$\begin{aligned}\vec{\mathbf{f}}_{q,n_q}&\left(k_x^{mn}, k_y^{mn}\right)\\ &= \frac{\mathrm{e}^{-j\left(k_{x0}x_{cq}+k_{y0}y_{cq}\right)}}{A}\int_{-L_q}^{L_q}\\ &\quad\times\left[\int_{l_{1q}\left(y'_q\right)}^{l_{2q}\left(y'_q\right)}\vec{f}_{q,n_q}\left(x'_q, y'_q\right)\mathrm{e}^{-j\left(k_{x0}x'_q+k_{y0}y'_q\right)}\right.\\ &\qquad\times\mathrm{e}^{-j\left(m\frac{2\pi b}{A}\left[\left(x'_q+x_{cq}\right)\sin\alpha_2-\left(y'_q+y_{cq}\right)\cos\alpha_2\right]\right)}\\ &\qquad\left.\times\mathrm{e}^{-j\left(n\frac{2\pi a}{A}\left[\left(y'_q+y_{cq}\right)\cos\alpha_1-\left(x'_q+x_{cq}\right)\sin\alpha_1\right]\right)}\mathrm{d}x'_q\right]\mathrm{d}y'_q. \quad (16)\end{aligned}$$

Numerical computation of (16) through the NUFFT requires its discretization in the canonical NUFFT form [12]

$$\vec{\mathbf{f}}_{q,n_q} \approx \sum_{k=0}^{N_S-1}\vec{\boldsymbol{\delta}}_{q,k}\mathrm{e}^{-j\left(m\mu_{q,k}+n\nu_{q,k}\right)}, \quad -M \leq m, n < M \quad (17)$$

where the truncation of m, n for the double infinite sum in (6) is now exposed.

Assuming $-L_q \leq y' \leq L_q$ is sampled in N_y points and $l_{1q}(y'_q) < x'_q < l_{2q}(y'_q)$ is sampled in N_x points, the sampling values are

$$y'_{q,i} = -L_q + (2i+1)L_q/N_y,\ x'_{q,ji} = l_{q1}\left(y'_{q,i}\right) + (2j+1)l_q^-\left(y'_{q,i}\right) \quad (18)$$

where $i = 0, \ldots, N_y - 1$ and $j = 0, \ldots, N_x - 1$. The total number of sampling points is $N_S = N_x N_y$, and the global index k can be computed as $k = i + jN_y$. By close inspection of (16)–(18), the values in (17) for the direct computation of $\vec{\mathbf{f}}_{q,n_q}$ through the NUFFT can be derived as

$$\begin{aligned}\vec{\boldsymbol{\delta}}_{q,k} &= \frac{4L_q\mathrm{e}^{-j\left(k_{x0}x_{cq}+k_{y0}y_{cq}\right)}}{N_x N_y A}l_q^-\left(y'_{q,i}\right)\vec{f}_{q,n_q}\left(x'_{q,ji}, y'_{q,i}\right)\\ &\quad\times\mathrm{e}^{-j\left(k_{x0}x'_{q,ji}+k_{y0}y'_{q,i}\right)} \quad (19)\\ \mu_{q,k} &= \frac{2\pi b}{A}\left[\left(x'_{q,ji}+x_{cq}\right)\sin\alpha_2 - \left(y'_{q,i}+y_{cq}\right)\cos\alpha_2\right] \quad (20)\\ \nu_{q,k} &= \frac{2\pi a}{A}\left[\left(y'_{q,i}+y_{cq}\right)\cos\alpha_1 - \left(x'_{q,ji}+x_{cq}\right)\sin\alpha_1\right]. \quad (21)\end{aligned}$$

III. Numerical Application Examples

Although the formulation presented in Section II is quite general and can be applied to a wide variety of FSSs alternating patches and apertures [6], for practical purposes we have chosen a geometrical shape that can yield a tightly packed FSS thanks to its inclusion in a skewed grid: the regular hexagon arranged in an equilateral triangular lattice. Fig. 2(b) shows a 2-D schematic of the proposed configuration, where hexagonal capacitive patches (in dashed green lines) are separated s_q for $q \in \mathbb{O}$, while inductive wire grids, generated by hexagonal apertures (in solid blue lines), have a width w_q for $q \in \mathbb{E}$. The corresponding unit cell is shown in the dotted red line, and it can easily be seen that $a = b$, $\alpha_1 = \pi/6$ and $\alpha_2 = \pi/2$. Please note that aperture centers are shifted with respect to patch centers (i.e., wire grid centers coincide with patch centers). This topology stems from [7], where squared patches and shifted squared apertures are alternated in a squared lattice. Since the objective of this work is to prove the efficiency and accuracy of the proposed formulation rather than a design procedure, most of the initial design steps (especially those regarding the reference circuit and the choice of design frequencies and materials) are taken from [7]. Thus, the dielectric material used for all the FSS layers is the Cer-10 material from Taconic corporation, with a relative permittivity of $\varepsilon_r = 10$ and a loss tangent of $\tan\delta = 0.0035$ in the employed frequency band. One important advantage of the FSS topology introduced in Fig. 2(b) over that reported in [7] is that the total area of the unit cell is reduced by a factor $\sin(\pi/3) = 0.866$ (86.6%), according to (10), if the same values of a and b are used. This means the overall size of the FSS can be eventually reduced if a similar response is achieved. To accomplish this goal, we have set $a = b = 3.5$ mm as in [7].

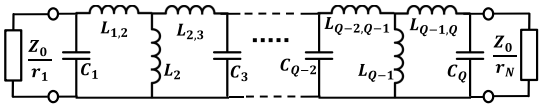

Fig. 3. Topology of the FSS equivalent circuit for bandpass filter responses.

Fig. 3 shows the topology of the reference equivalent circuit used as the initial design step of the FSS. The response of this circuit (lossless) will be used to check the response of the final FSS designed. The topology of Fig. 3 is meant for an Nth order filter, so that the number of nonresonant elements amounts to $Q = 2N - 1$. In all considered cases, Z_0 is the free space impedance and the normalized source and load impedances are $r_1 = r_N = 1$ since an odd value of N has always been used. For the design of the FSS, we follow the procedure described in [7] starting from an Nth order bandpass coupled resonator filter. Normalized values for quality factors of the first and last resonator as well as the coupling coefficients between the resonators can be found in [13].

In order to prove the efficiency of the formulation proposed in this communication, we have made a comparison between the CPU time required by our in-house software and that required by the general-purpose commercial software CST Microwave Studio (CST MWS), specifically with the use of its frequency solver. To estimate the CPU time required by CST MWS, we have considered the average time taken by each discrete frequency point once the mesh adaptation process is finished (i.e., the time taken by each discrete frequency point for the final mesh which ensures convergence). The implementation of our formulation has been coded in Fortran. All simulations are performed in a desktop computer with Intel Core i7-7700 CPU at 3.6 GHz with 32 GB RAM (and Microsoft Windows 10).

A. Third-Order Bandpass FSS

The first design considered is a third-order bandpass FSS with a 0.1 dB ripple Chebychev response, a center frequency of 10.82 GHz, and a fractional bandwidth of 21.7%. These specifications are found in [7], where, as said, the steps to calculate the equivalent circuit parameters shown in Table I are described. The thickness of each Taconic Cer-10 layer is chosen as 0.64 mm among the commercial available values.

For the analysis of the structure, the double summations in (6) are truncated to 8100 terms (corresponding to setting $M = 45$ in (17)), the same as the total number of sampling points for the NUFFT. In all metallizations levels ($q = 1, \ldots, 5$) the number of basis functions is set to $N_q = 32$ (corresponding to $N_q^{1r} = N_q^{1s} = N_q^{2r} = N_q^{2s} = 4$). Regarding the design, the initial parameters for the FSS are set to

Authorized licensed use limited to: Universidad de Sevilla. Downloaded on July 23,2024 at 15:02:16 UTC from IEEE Xplore. Restrictions apply.

TABLE I
THIRD-ORDER BANDPASS CIRCUITAL AND FSS PARAMETERS

Parameter	C_1,C_5	L_2,L_4	C_3	$L_{1,2}$,$L_{4,5}$	$L_{2,3}$,$L_{3,4}$
Value	257.6 fF	177.0 pH	520.5 fF	699.0 pH	690.1 pH

Parameter	s_1,s_5	w_2,w_4	s_3	$h_q, q = 1 \ldots 4$
Value	0.359 mm	1.386 mm	0.317 mm	0.64 mm

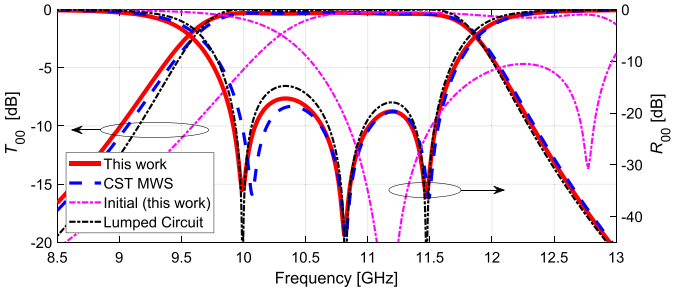

Fig. 4. T_{00} and R_{00} of the third-order bandpass FSS for normal incidence.

$s_1 = s_3 = s_5 = 0.5$ mm and $w_2 = w_4 = 1.3$ mm. With these values, the transmission and reflection responses of the FSS for normal incidence ($\theta_{\text{inc}} = 0°$), coincident for TM_z and TE_z, are shown in dashed-dotted magenta line in Fig. 4. As can be seen, it is far away from the desired circuital response, shown in the dashed-dotted black line in Fig. 4. From these initial design values, a simple design strategy is followed which consists of varying the values of the geometrical parameters s_1, w_2, s_3, w_4, and s_5 until the three poles of the full-wave FSS reflection response for normal incidence match those of the circuital response, which are located at 9.992, 10.82, and 11.47 GHz. For that purpose, we include the MoM analysis inside an optimization routine, namely the BOBYQA algorithm [14], to minimize the sum of the magnitude of the reflection at those frequencies. We would like to point out that this full-wave optimization is possible because of the efficiency of the proposed spectral MoM NUFFT-based formulation, which only requires around 8.1 s for the evaluation of one cost function. The optimization algorithm just takes 86 cost function evaluations to yield the values for s_1, w_2, s_3, w_4, and s_5 shown in Table I. The overall response of the FSS is shown in the red solid line in Fig. 4. To crosscheck the obtained results, a simulation of the final structure has been carried out in CST MWS. The result is shown in the dashed blue line in Fig. 4.

To further cross-check the capabilities of the proposed method, the designed FSS is simulated at an oblique incidence angle of $\theta_{\text{inc}} = 45°$. The transmission and reflection responses (equal for $\phi_{\text{inc}} = 0°$ and 90°), together with those achieved by CST MWS, are shown in Fig. 5 for both TM_z and TE_z incidence. As demonstrated in [7] for squared lattices, the small overall profile and the small unit cell size of this FSS make it possible to keep the filtering response for oblique incidence (in this particular case, also without cross-coupling between TM_z and TE_z fields in the two main planes $\phi_{\text{inc}} = 0°$ and 90°).

Figs. 4 and 5 show a high level of agreement between the results of our in-house software and those of CST MWS. However, the CPU time per frequency point required by our proposed formulation is roughly 2.7 s, which is on average 36 times shorter than that required by CST MWS.

B. Fifth-Order Bandpass FSS

An FSS showing a fifth-order Chebychev response with 0.1 dB ripple and 37% fractional bandwidth at 12 GHz has also been designed

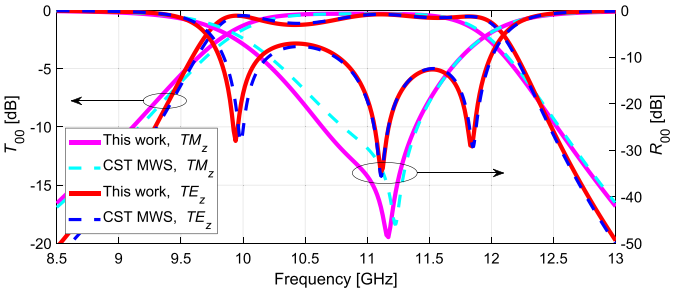

Fig. 5. T_{00} and R_{00} of the third-order bandpass FSS for $\theta_{\text{inc}} = 45°$.

TABLE II
FIFTH-ORDER BANDPASS CIRCUITAL AND FSS PARAMETERS

Parameter	C_1,C_9	L_2,L_8	C_3,C_7	L_4,L_6	C_5
Value	123.9 fF	545.3 pH	300.0 fF	679.5 pH	200.0 fF
Parameter	$L_{1,2}$,$L_{8,9}$	$L_{2,3}$,$L_{7,8}$	$L_{3,4}$,$L_{6,7}$	$L_{4,5}$,$L_{5,6}$	
Value	1095 pH	802.4 pH	720.6 pH	1409 pH	

Parameter	s_1,s_9	w_2,w_8	s_3,s_7	w_4,w_6	s_5
Value	1.450 mm	0.788 mm	0.862 mm	0.724 mm	1.428 mm
Parameter	h_1, h_4, h_5, h_8		h_2, h_3, h_6, h_7		
Value	1.27 mm		0.76 mm		

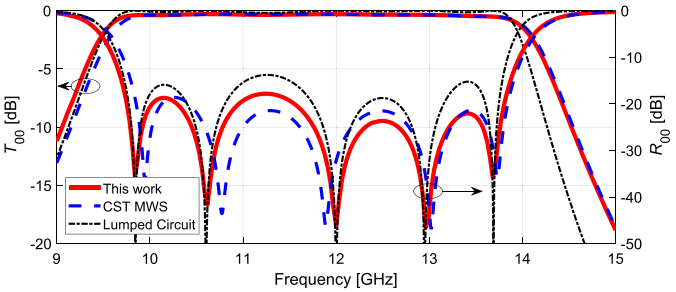

Fig. 6. T_{00} and R_{00} of the fifth-order bandpass FSS for normal incidence.

to prove that the proposed formulation can handle a high number of layers. The reference lumped-element values for this fifth-order response are shown in Table II. These values generate an ideal circuital response shown in the dashed-dotted black line in Fig. 6. The FSS to be designed has a total of nine layers for the corresponding nine nonresonant elements. In this case, fine-tuning manual steps have been combined with the aforementioned optimization routine to estimate the geometrical parameters that match the frequency poles of the circuit response for normal incidence. In the initial iterations of the optimization process, the thickness of dielectric layers have also been considered as design variables, and then fixed to the closest available commercial thicknesses. Overall, several hundreds of evaluations of the cost function have been performed to yield the values shown in Table II. The achieved FSS transmission and reflection responses for normal incidence are shown in solid red line in Fig. 6, together with that provided by CST MWS (dashed blue line). Good agreement is found between the two sets of results. It can be seen that our simulation results for the FSS response share the frequency poles of the circuital response. Interestingly, the computational demand for the analysis of this fifth-order FSS with both our software and CST MWS is lower than in the case of the previously described third-order FSS. This can be explained by the fact that nonresonant elements are further away from each other, and thus the requirements to accurately model EM interactions between them are diminished. Specifically, although in all metallization levels

Authorized licensed use limited to: Universidad de Sevilla. Downloaded on July 23,2024 at 15:02:16 UTC from IEEE Xplore. Restrictions apply.

($q = 1, \ldots, 9$) the number of basis functions has also been set to $N_q = 32$ (as in the previous example), in this case the double summation in (6) is truncated to 3600 terms (corresponding to setting $M = 30$ in (17)). With these settings, our proposed implementation takes an average time of 2.16 s per frequency point, which is about 13 times shorter than the average time taken per frequency point by CST MWS. As previously stated, meshing operations of CST MWS have not been considered in this comparison, but for this particular structure the meshing time is not negligible, and should be considered when facing a design of this type with CST MWS.

IV. Conclusion

A specific formulation is developed for the application of the spectral MoM to the efficient analysis of multilayered periodic structures alternating patches and apertures. The formulation is especially useful for the design of high-order bandpass FSSs made up of solid-interior type nonresonant elements. With the objective of analyzing arrangements with tightly packed complex shaped elements within reasonable CPU times, edge-singularity basis functions are used to approximate the electric currents/tangential electric fields on the patches/apertures in the case where the grid of the periodic structures can be skewed. Since the Fourier transforms of the basis functions cannot be obtained in closed form, these Fourier transforms are computed by means of the NUFFT, which is adapted to deal with the particular case of skewed grids treated in this communication. As a practical application of the software implemented, a four-layer FSS and an eight-layer FSS made up of alternating hexagonal patches and apertures arranged in a triangular lattice have been designed to synthesize, respectively, a third-order and a fifth-order Chebychev bandpass response. For validation purposes, the designed FSSs have been analyzed with both our in-house software and commercial software CST MWS, and good agreement has been found. Although the formulation presented in this communication for a specific problem may be more cumbersome to implement than the use of commercial software, the results indicate that the developed software can provide the design of sophisticated FSSs, including many dielectric layers and metallization levels with both patches and apertures, within a few hours in a personal computer, whereas it may take a few days with commercial software. This speedup factor compensates for the effort carried out, thus paving the way to use the proposed formulation in future complex FSS designs with stringent specifications.

References

[1] R. Mittra, C. H. Chan, and T. Cwik, "Techniques for analyzing frequency selective surfaces–A review," *Proc. IEEE*, vol. 76, no. 12, pp. 1593–1615, Dec. 1988.

[2] J. C. Vardaxoglou, *Frequency Selective Surfaces: Analysis and Design*. Research Studies Press, 1997.

[3] B. A. Munk, *Frequency Selective Surfaces: Theory and Design*. Hoboken, NJ, USA: Wiley, 2000.

[4] A. M. Lerer and A. G. Schuchinsky, "Full-wave analysis of three-dimensional planar structures," *IEEE Trans. Microw. Theory Techn.*, vol. 41, no. 11, pp. 2002–2015, Nov. 1993.

[5] A. G. Schuchinsky, D. E. Zelenchuk, A. M. Lerer, and R. Dickie, "Full-wave analysis of layered aperture arrays," *IEEE Trans. Antennas Propag.*, vol. 54, no. 2, pp. 490–502, Feb. 2006.

[6] M. Camacho, R. R. Boix, and F. Medina, "NUFFT for the efficient spectral domain MoM analysis of a wide variety of multilayered periodic structures," *IEEE Trans. Antennas Propag.*, vol. 67, no. 10, pp. 6551–6563, Oct. 2019.

[7] M. A. Al-Joumayly and N. Behdad, "A generalized method for synthesizing low-profile, band-pass frequency selective surfaces with non-resonant constituting elements," *IEEE Trans. Antennas Propag.*, vol. 58, no. 12, pp. 4033–4041, Dec. 2010.

[8] R. Florencio, R. R. Boix, and J. A. Encinar, "Fast and accurate MoM analysis of periodic arrays of multilayered stacked rectangular patches with application to the design of reflectarray antennas," *IEEE Trans. Antennas Propag.*, vol. 63, no. 6, pp. 2558–2571, Jun. 2015.

[9] R. Pous and D. M. Pozar, "A frequency-selective surface using aperture-coupled microstrip patches," *IEEE Trans. Antennas Propag.*, vol. 39, no. 12, pp. 1763–1769, Dec. 1991.

[10] F. L. Mesa, R. Marques, and M. Horno, "A general algorithm for computing the bidimensional spectral Green's dyad in multilayered complex bianisotropic media: The equivalent boundary method," *IEEE Trans. Microw. Theory Techn.*, vol. 39, no. 9, pp. 1640–1649, Sep. 1991.

[11] M. Camacho, R. R. Boix, and F. Medina, "Computationally efficient analysis of extraordinary optical transmission through infinite and truncated subwavelength hole arrays," *Phys. Rev. E, Stat. Phys. Plasmas Fluids Relat. Interdiscip. Top.*, vol. 93, no. 6, Jun. 2016, Art. no. 063312.

[12] L. Greengard and J.-Y. Lee, "Accelerating the nonuniform fast Fourier transform," *SIAM Rev.*, vol. 46, no. 3, pp. 443–454, Jan. 2004.

[13] A. I. Zverev, *Handbook of Filter Synthesis*. Hoboken, NJ, USA: Wiley, 1967.

[14] M. Powell, "The BOBYQA algorithm for bound constrained optimization without derivatives," Dept. Appl. Math. Theor. Phys., Cambridge Univ., Cambridge, U.K., Tech. Rep. DAMTP 2009/NA06, 2009.

Authorized licensed use limited to: Universidad de Sevilla. Downloaded on July 23,2024 at 15:02:16 UTC from IEEE Xplore. Restrictions apply.